Mon. Not. R. Astron. Soc. **383,** 1259–1268 (2008) doi:10.1111/j.1365-2966.2007.12633.x

Constraints on the average magnetic field strength of relic radio sources 0917+75 and 1401−33 from *XMM–Newton* observations

C. M. Hubert Chen,[1⋆] D. E. Harris,[2⋆] Fiona A. Harrison[1⋆] and Peter H. Mao[1⋆†]
[1]*Department of Physics, California Institute of Technology, Pasedena, CA 91125, USA*
[2]*Harvard–Smithsonian Center for Astrophysics, 60 Garden Street, Cambridge, MA 02138, USA*

Accepted 2007 October 24. Received 2007 October 23; in original form 2007 August 4

ABSTRACT

We observed two relic radio sources, 0917+75 and 1401−33, with the *XMM–Newton* X-ray observatory. We did not detect any X-ray emission, thermal or non-thermal, in excess of the local background level from either target. This imposes new upper limits on the X-ray flux due to inverse Compton scattering of photons from the cosmic microwave background by relativistic electrons in the relic sources, and new lower limits on the magnetic field strength from the relative strength of the radio and X-ray emission. The combination of radio and X-ray observations provides a measure of the magnetic field independent of equipartition or minimum energy assumptions. Due to increasing sensitivity of radio observations, the known population of cluster relics has been growing; however, studies of non-thermal X-ray emission from relics remain scarce. Our study adds to the small sample of relics studied in X-rays. In both relics, our field strength lower limits are slightly larger than estimates of the equipartition magnetic field.

Key words: radiation mechanisms: non-thermal – galaxies: magnetic fields – radio continuum: galaxies – X-rays: galaxies.

1 INTRODUCTION

In a minority of clusters of galaxies, there are isolated diffuse sources of radio emission with steep spectra and without definite associations with an optical galaxy counterpart. These sources are classified as haloes or relics, depending on their location and size: haloes reside at the centre of a cluster of galaxies, and are usually circular and not known to be highly polarized. In contrast, relics are found in cluster outskirts, and are often elongated and linearly polarized. Given the general phenomenological designation, the term 'relic' actually refers to a few different and probably distinct types of sources, including old radio lobes from dead radio galaxies and regions where particles are re-accelerated in cluster mergers (Giovannini & Feretti 2004; Kempner et al. 2004). Statistics on relics are growing; to date, over 30 relics have been discovered.

The various types of relics share common observational characteristics, including a power-law radio spectrum, indicative of synchrotron emission by relativistic particles in a magnetic field. The radio spectrum alone constrains only the product of the magnetic field and particle density. The standard approach to estimating the magnetic field strength and particle density individually is to assume minimum energy or equipartition of energy densities between the two components. A direct observational approach is to measure the non-thermal X-ray spectrum due to inverse Compton scattering of photons from the cosmic microwave background (IC/CMB) by relativistic particles in the relic (Harris & Grindlay 1979). This provides a measurement of the particle density, and thus decouples the contributions of magnetic field and particles to the synchrotron flux.

While IC/CMB measurements have been made on other, stronger radio sources of synchrotron emission (e.g. Croston et al. 2005), IC/CMB measurements on relics remain scarce. The difficulty stems from the weak and diffuse nature of relic emission, as well as contamination by thermal emission, often from a nearby cluster. To date, there are only three claims of IC/CMB detections in relic radio sources (Bagchi, Pislar & Lima Neto 1998; Fusco-Femiano et al. 2003; Kempner, Sarazin & Markevitch 2003), but the statistics are poor, and later studies refute two of these detections (Henriksen, Hudson & Tittley 2004; Durret, Lima Neto & Forman 2005). For a number of other relics, non-detections have yielded lower limits on the magnetic field strength. Further X-ray measurements with sensitivity improvement over past studies are interesting, as they strengthen the constraints on the magnetic field and particle content in relics.

In this paper we present *XMM–Newton* observations of two relics, 0917+75 and 1401−33. Our X-ray observations are the most sensitive to date for these sources. Combined with previous radio

⋆E-mail: hubert@caltech.edu (CMHC); harris@head.cfa.harvard.edu (DEH); fiona@srl.caltech.edu (FAH); peterm@ess.ucla.edu (PHM)
†Present address: Department of Earth and Space Sciences, University of California, Los Angeles, 595 Charles Young Drive East, Box 951567, Los Angeles, CA 90095-1567, USA.

Table 1. Source and XMM observation parameters.

Target	0917+75	1401−33	
Right ascension (J2000)	$09^{\rm h}22^{\rm m}11\overset{\rm s}{.}40$	$14^{\rm h}04^{\rm m}16\overset{\rm s}{.}70$	
Declination (J2000)	$74^\circ59'31\overset{''}{.}00$	$-34^\circ02'22\overset{''}{.}00$	
Angular size (arcmin^2)	4×8	9×20	
Galactic H I column density, $n_{\rm H}$	2.09×10^{20}	5.44×10^{20}	cm^{-2}
Cosmological redshift, z	0.125	0.0136	
XMM observation date	2002 March 20 07:00:21.0 UT	2002 February 14 07:59:00.0 UT	
XMM observation length	26 744	20 433	s

observations, we derive constraints on their magnetic field and particle content. Section 2 describes the X-ray and radio data, Section 3 details our analysis, and Section 3.2.3 presents the numerical results. We discuss each source individually in Section 4, and give a summary of our findings in Section 5. We adopt the currently accepted cosmology with $H_0 = 70\,{\rm km\,s^{-1}\,Mpc^{-1}}$, $q_0 = -0.55$ and $\Omega_\Lambda = 0.7$. At $z = 0.125$ and 0.0136, respectively, the distances to 0917+75 and 1401−33 are 502 and 57.8 Mpc, and the linear scales are 134 and 16.7 kpc arcmin^{-1}.

2 THE OBSERVATIONS

We observed each of the targets, 0917+75 and 1401−33, in a ∼20-ks pointing with *XMM–Newton*. We obtained radio images of the targets at 1.4 GHz from the NRAO VLA Sky Survey (NVSS) catalogue (Condon et al. 1998), via the *SkyView* facility (McGlynn, Scollick & White 1996).[1] We also used published data from Harris et al. (1993) and Goss et al. (1987). Table 1 lists some properties of the targets and the parameters of the observations.

3 DATA ANALYSIS

We first reprocessed the X-ray data sets using the routines emproc and epproc in the *XMM–Newton* Science Analysis Software (SAS), version 6.5.0.

Then, we filtered the processed data based on temporal, spectral, and spatial criteria, as described below.

3.1 Event filtering

For temporal filtering, we generated good-time intervals (GTIs) based on the double-filtering technique described in appendix A of Nevalainen, Markevitch & Lumb (2005): we inspected light curves of high-energy events (above 9.5 keV for MOS and 10.0 keV for PN) of 1-ks resolution, and screened out time intervals where the high-energy count rate at any of the three detectors exceeded 120 per cent of the mean level. We also inspected light curves of events within 1–5 keV at the periphery of the field of view ($12 < r < 15$ arcmin, r being the distance from the nominal pointing direction), and screened out time intervals where any of the count rates, summed over the periphery annulus, exceeded mean + 0.028 counts s^{-1} for MOS and mean + 0.056 counts s^{-1} for PN. The final GTI for each observation is the intersection of the GTIs from the high- and low-energy filters. It is about 89 per cent the length of the entire observation for 0917+75, and about 80 per cent for 1401−33. Table 2 lists the temporal filtering parameters in detail.

We restricted the region for photon extraction to coincide with the radio source extent, and we filtered out regions containing point source detections. From the NVSS radio image of each target, we made a mask by selecting only pixels in the vicinity of the target whose flux densities are at least 5σ above the background level in each image. To mask out X-ray point sources in each field, we took the three source lists (one from each detector on *XMM–Newton*) provided with the pipeline products, and ran them through the SAS routine region. This produced three FITS region files for each field, specifying regions that excluded all the detected point sources, with the size of each excluded region determined by the level of flux for that particular source. We combined the radio mask and X-ray point source regions to form the spatial filtering expression for each of the targets. These masks are shown in Figs 1 and 2.

We determined the optimal energy band for signal extraction by comparing (1) the expected source flux density at equipartition and (2) the average background for *XMM–Newton* at various energies. To estimate the source flux density at equipartition, we followed the analytical formulation in Harris & Grindlay (1979) and deduced a power-law model for the IC/CMB emission from each source, with model parameters based on data from past radio observations (Harris et al. 1993). Tables 1 and 3 lists these parameters. To estimate the background, we took blank-sky event files obtained from the web site of the *XMM–Newton* Science Operation Centre[2] as representative background measurements, and computed a background spectrum from the files. Carter & Read (2007) described these blank-sky data sets in detail. With these source and background spectra, we selected an energy band [$E_{\rm min}$, $E_{\rm max}$] and calculated the signal-to-noise ratio (S/N) associated with the band. We then varied $E_{\rm min}$ and $E_{\rm max}$ at 0.1-keV increments until we obtained the energy band with the maximum S/N. Using this method, we arrived at the optimal MOS bands 0.2–3.7 keV for 0917+75 and 0.2–6.5 keV for 1401−33. Table 2 shows the selected energy bands for PN as well.

In addition to the GTIs and energy bands obtained as described above, we further applied the following event filtering expressions: (FLAG == 0 && PATTERN <= 12) for MOS and (FLAG == 0 && PATTERN <= 4) for PN. These expressions retained only events triggering 1 or 2 pixels, and only those flagged as valid by the standard processing routines. From the filtered event list, we generated images and exposure maps. We then used the masks and regions described above to select the region of sky corresponding

[1] http://skyview.gsfc.nasa.gov/

[2] http://xmm.vilspa.esa.es/external/xmm_sw_cal/background/blank_sky.shtml

Table 2. Numerical results from the X-ray observations.

Target	0917+75			1401−33			
Detector	MOS1	MOS2	PN	MOS1	MOS2	PN	
Observation mode	Full window	Full window	Extended full window	Full window	Full window	Extended full window	
Filter	Medium	Medium	Medium	Medium	Medium	Medium	
Hard-band count rate	0.188–0.378	0.207–0.383	0.770–1.65	0.152–0.208	0.151–0.237	0.560–0.805	counts s^{-1}
Mean	0.247	0.259	0.962	0.184	0.188	0.671	counts s^{-1}
Soft-band annulus count rate	0.119–0.202	0.118–0.190	0.210–0.340	0.166–0.266	0.177–0.251	0.368–0.516	counts s^{-1}
Mean	0.148	0.150	0.262	0.214	0.216	0.446	counts s^{-1}
Observation length	27 825	27 824	23 792	19 327	19 326	15 291	s
Flare-filtered length	24 715	24 720	20 693	15 483	15 484	12 082	s
Good-time fraction	89	89	87	80	80	79	per cent
Optimal energy band	0.2–3.7	0.2–3.7	0.2–2.3	0.2–6.5	0.2–6.5	0.2–4.1	keV
Source region							
Event count in this study, optimal band	444	405	1441	488	529	1244	events
in blank-sky data, optimal band	–	–	–	10 122	9840	24 308	events
in this study, hard band	–	–	–	40	42	120	events
in blank-sky data, hard band	–	–	–	1403	1432	6698	events
Exposure map, median	24 054.6	23 764.0	17 680.7	14 218.5	14 594.4	10 030.4	s
Mean	23 847.3	23 061.4	16 870.2	14 064.4	14 295.8	9850.77	s
Number of 4.35 arcsec pixels	1856	1856	1785	1406	1406	1384	pixels
Event rate[a]	0.0186	0.0176	0.0854	0.0142	0.0168	0.0821	counts s^{-1}
Background region							
Event count in this study, optimal band	352	383	1196	739	868	1840	events
in blank-sky data, optimal band	–	–	–	16 422	17 797	41 911	events
in this study, hard band	–	–	–	63	80	230	events
in blank-sky data, hard band	–	–	–	3159	3751	11 558	events
Exposure map, median	19 570.7	19 612.4	14 241.8	6043.56	6656.07	4656.47	s
Mean	19 268.2	19 505.8	13 634.9	5976.04	6701.31	4615.42	s
Number of 4.35 arcsec pixels	1881	1881	1763	3128	3208	3096	pixels
Event rate[a], Scaled to source region	0.0180	0.0194	0.0888	0.0310	0.0319	0.0974	
	±0.0016	±0.0015	±0.0016	±0.0043	±0.0035	±0.0129	counts s^{-1}
Source count rate, 3σ upper limit	$\leqslant 4.70 \times 10^{-3}$	$\leqslant 4.59 \times 10^{-3}$	$\leqslant 4.78 \times 10^{-2}$	$\leqslant 1.28 \times 10^{-2}$	$\leqslant 1.05 \times 10^{-2}$	$\leqslant 3.86 \times 10^{-2}$	counts s^{-1}
(MOS co-added)	$\leqslant 3.86 \times 10^{-3}$			$\leqslant 1.11 \times 10^{-2}$			counts s^{-1}

[a]Event rates are blank-sky subtracted for 1401−33 but not for 0917+75. See text for details.

to each target. The total counts divided by the mean of the exposure map in the selected region gave the event rate.

3.2 Background determination and flux upper limit analysis

The two observations in this paper pose very different challenges for background determination. We discuss our approach for each observation separately in the following.

3.2.1 0917+75

For 0917+75, the time of our observation unfortunately coincided with a coronal mass ejection (CME) from the Sun. Snowden, Collier & Kuntz (2004) reported an enhancement in the *XMM–Newton* background, especially at 0.5–1.0 keV, concurrent with an enhancement in the solar wind measured by the *Advanced Composition Explorer* (*ACE*) and other monitoring spacecraft. When we obtained data from *ACE*[3] and inspected the light curves at the time of our observations (Fig. 3), we found that our observation of 0917+75 coincided with an episode of significant enhancement of the O^{7+}/O^{6+} ratio in the solar wind, characteristic of a CME (R. C. Ogliore, private communication).

To assess the impact of this event on the background level in our observation, we compared the event rate in our data set with the rates in two standard blank-sky data sets independent of our observation: one set was from Nevalainen et al. (2005) and the other from Carter & Read (2007). We chose these two sets because we employed the flare-filtering recipe of Nevalainen et al. (2005) in this study, while Carter & Read (2007) provides a much larger data set, with better event statistics. We refiltered the Carter & Read (2007) data set with the (FLAG == 0) expression so that comparison of the three data sets is consistent. However, we have not refiltered the Carter & Read (2007) data set for flares using the recipe in Nevalainen et al. (2005), as its full view hard-band event rates (0.26 and 2.7 counts s^{-1} for MOS and PN, respectively) are above the range deemed consistent with the sample of Nevalainen et al. (2005), making the hard-band filtering method inapplicable. To minimize the variability of any other systematic parameters (such as vignetting), we applied the masks and regions that we obtained for the source regions of 0917+75 in this blank-sky measurement, thus selecting the same detector pixels. We computed count rates at various energies from the filtered blank-sky event files, and compared them with our

[3] http://www.srl.caltech.edu/ace/ASC/.

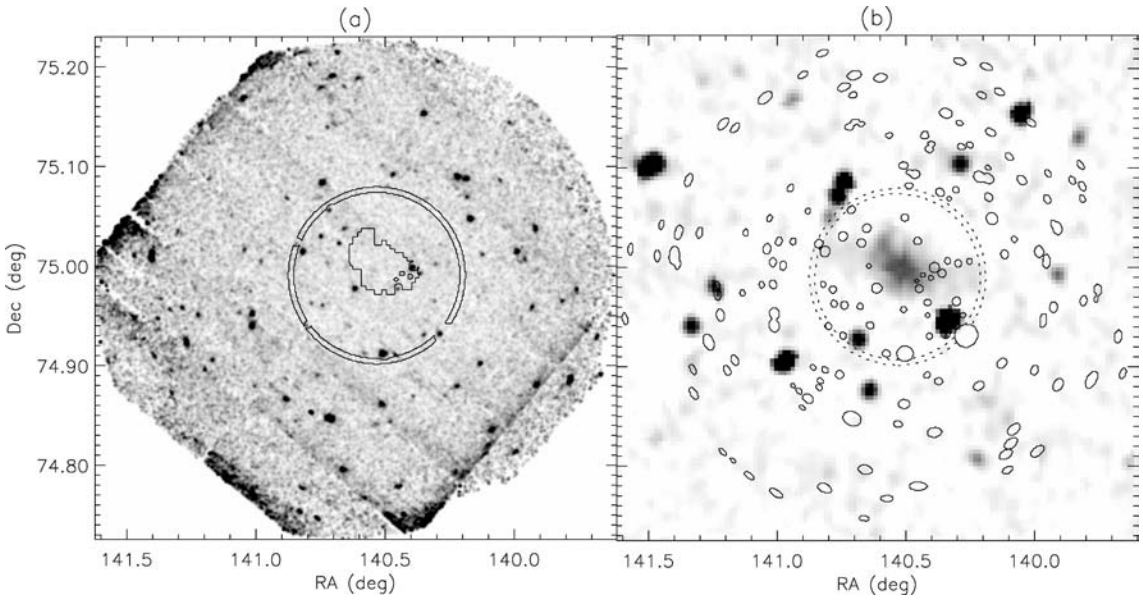

Figure 1. *XMM–Newton* (a) and NVSS (b) images of 0917+75. The two images have the same spatial extent. The source (centre) and background (annulus) regions are indicated by solid lines in (a); the background region is also shown in (b) by dotted lines. X-ray point sources detected within the *XMM–Newton* field of view are marked by solid lines in (b), with the size of each region proportional to the X-ray flux of the point source. The boundary of the source region is identical to the mean + 5σ contour in the NVSS image, excluding all overlapping X-ray point source regions. Image (a) is made by (1) scaling the filtered MOS (0.2–3.7 keV) and PN (0.2–2.3 keV) images, according to each instrument's response to the same source model and flux, (2) correcting the scaled images for exposure and combining them with the SAS routine emosaic and (3) smoothing the combined image with a Gaussian function of width $\sigma = 4$ arcsec, about the size of the instrument's point spread function.

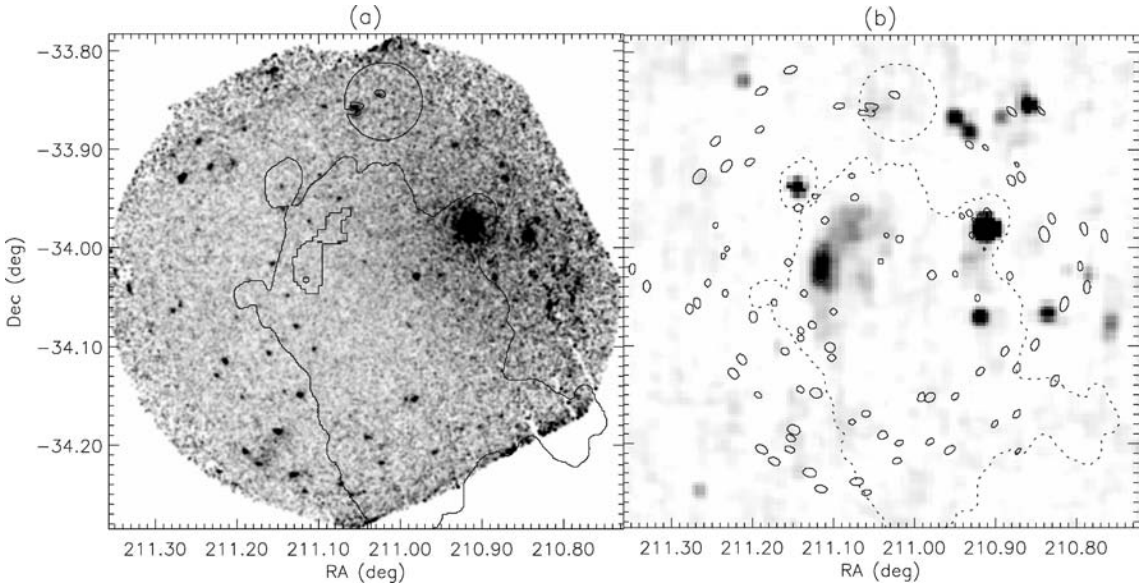

Figure 2. *XMM–Newton* (a) and NVSS (b) images of 1401−33. See Fig. 1 for a description of the various features. In addition to the source and background regions at the centre and top of the images, respectively, we also mark the extent of the radio emission at 330 MHz, according to fig. 1 in Subrahmanyan et al. (2003). Note that the source and background regions here are equidistant from the bright galaxy NGC 5419 at the centre of the Abell S753 cluster, about 10 arcmin to the west (right-hand side) of the source region. Image (a) combines the filtered MOS images of 0.2–6.5 keV and the filtered PN image of 0.2–4.1 keV.

source region count rates for 0917+75, both without exposure-map correction. Fig. 4 shows spectra of 0917+75 and of the blank-sky data thus obtained. It shows that the continuum level in our observation of 0917+75 is consistent with that from Nevalainen et al. (2005), but lower than the level from Carter & Read (2007). We believe the difference between the two blank-sky data sets is due to different levels of flare filtering. As we employed the more stringent double-GTI filtering recipe of Nevalainen et al. (2005) in this study, our spectrum of 0917+75 should be directly comparable with a spectrum of the same detector region made from their data set. We note that the CME during our observation explains the excess line emission (relative to the continuum) at multiple energies below 1.0 keV in the spectrum of 0917+75, which is not seen in either blank-sky spectrum.

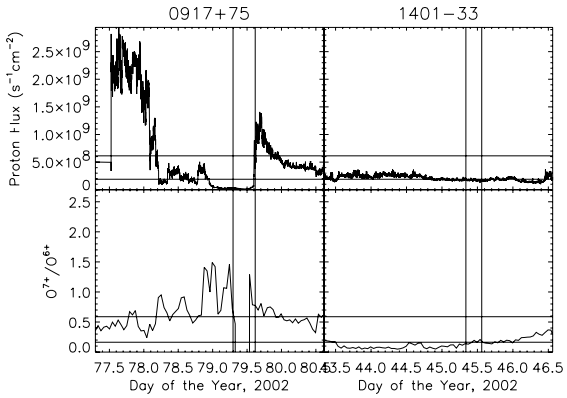

Figure 3. Proton flux and ratio of oxygen charge states O^{7+}/O^{6+} in the solar wind, measured by *ACE* during the time of our observations. The two horizontal lines in each panel indicate the mean and 90th percentile levels of each quantity over the first 100 d of 2002. The two vertical lines in each panel delimit the period of the *XMM–Newton* observation. The 64-s averaged proton flux data are from the SWEPAM instrument on *ACE*, while the hourly charge state ratios are from the SWICS/SWIMS instrument. Note that the break in the O^{7+}/O^{6+} curve at the time of our observation of 0917+75 was due to missing data. Yet, from the values before and after the break, one can infer that the O^{7+}/O^{6+} ratio during the observation is probably higher than the 90th percentile. There is a ∼1 h traveltime by the solar wind from the L1 point, the location of *ACE*, to the Earth. The time shown here is the time measured by *ACE*.

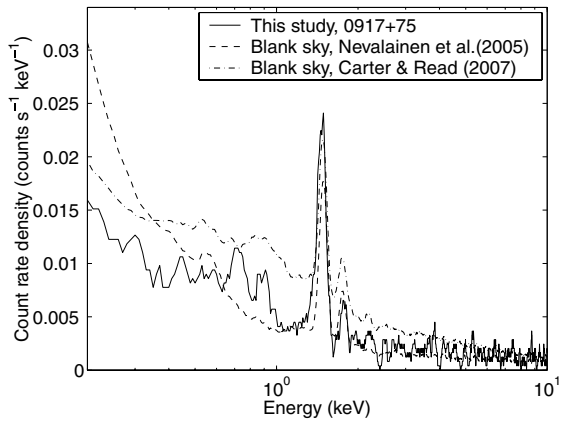

Figure 4. Spectra of 0917+75 and of the blank-sky data. The solid line shows the spectrum of 0917+75 from MOS2, convolved with a 100-eV wide boxcar. The dashed and dash–dotted lines show the blank-sky spectra (also convolved with a 100-eV wide boxcar) from Nevalainen et al. (2005) and from Carter & Read (2007), respectively. Both blank-sky spectra contain events extracted from the same detector coordinates of MOS2 as the source region in this study, and scaled to the spectrum of 0917+75 by equating the GTI-filtered lifetimes. Data from Carter & Read (2007) is also refiltered with (FLAG == 0) for consistent comparison. Note the excess of counts at discrete 'spectral lines' at 0.5–1.0 keV when compared to the data from Nevalainen et al. (2005), and the overall deficit of counts when compared to Carter & Read (2007) (see text for an explanation). The count rates displayed here are lifetime corrected.

To further investigate this background discrepancy, we looked at light curves generated from our observation of 0917+75. Fig. 5 shows the light curves of all events above about 10 keV from the entire field of view, which we generated to determine the high-energy GTIs (see Section 3.1). This figure shows that the count rates over the entire field of view above about 10 keV were above the 'acceptable' range of high-energy particle background rate reported by Nevalainen et al. (2005) for the majority of our observation period, and for all three detectors. This is evidence that our entire observation was plagued with low-amplitude long-duration flares, and that residual flares still lurk in the background after our double-GTI filtering. Thus, these light curves are consistent with the *ACE* data, suggesting an elevated background.

Because our observation was contaminated by flares, count rates from blank-sky data sets do not correctly reflect the nature of the background in our data. Besides, according to Fig. 4, the source rate in our data does not exceed the blank-sky count rates. Both of these reasons make it impossible for us to use blank-sky data for quantitative background subtraction. Thus, we measured the background level and its variation (for setting a flux limit in the case of non-detection) solely from multiple local background regions. We obtained the local background regions using a similar approach as we did for the source regions, applying temporal and spectral filters described in Section 3.1. For the spatial filters, we inspected the radio image of 0917+75 from NVSS, as well as X-ray images from the pipeline products, to find regions of sky within the *XMM–Newton* field of view but securely outside the target, as seen in radio frequencies, and where there are few detectable X-ray point sources. We selected an annulus immediately outside the target, with area similar to the source region. This annulus is inscribed within the central CCDs of MOS1 and MOS2, which simplifies the comparison between the source and background regions, as potentially different background levels at different CCDs (Pradas & Kerp 2005) become irrelevant for the two MOS modules. With the background region thus selected, we excluded X-ray point sources from the region in the same way as was done for the source region. Fig. 1 shows the resulting background annulus. We then applied this local background region to the filtered images and exposure maps described in Section 3.1, and obtained the total background count, mean exposure, and background count rate scaled to the total exposure in the source region. To assess the variation of the background level in our observation, we obtained additional background regions in the vicinity of the annulus and scaled the event rates within them in a similar fashion, and calculated the standard deviation σ of scaled event rates in this sample.

To assess the amount of degradation in our data due to residual flares, we calculated the count rates of individual pointings that make up the blank-sky data set of Nevalainen et al. (2005). We then compared the background variation (over space) in our data with the variation of the blank-sky count rates (over time). We found the variation in our background to be greater than that in the blank-sky data by factors of 1.26, 1.27 and 2.05 for the MOS1, MOS2 and PN detectors, respectively. The flux limit we set in this study is affected accordingly.

3.2.2 1401−33

Compared to 0917+75, the nature of the background in our observation of 1401−33 is quite different. The observation was made at a time of average solar wind activity, as shown by *ACE* data during this period (see Fig. 3); the overall count rates above about 10 keV are also well within the accepted quiescent levels. However, an X-ray halo of thermal emission centred at the neighbouring bright galaxy NGC 5419 about 10 arcmin away west of north-west (Subrahmanyan et al. 2003) dominates the local background, producing excess flux across the entire field of view when compared to blank-sky data. This thermal emission is so strong that spectral lines

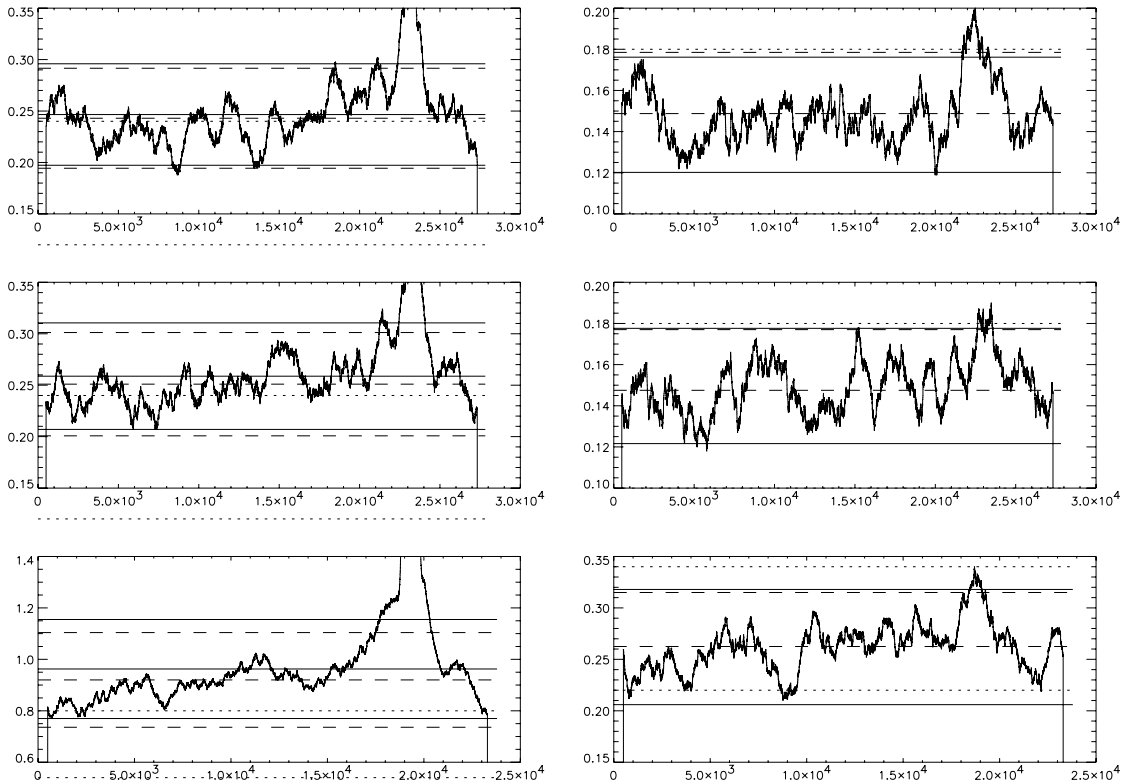

Figure 5. Light curves of high-energy events (left-hand panels) and of events at the periphery of the field of view (right-hand panels) during the observation of 0917+75. The three rows of graphs show, from top to bottom, events from MOS1, MOS2 and PN, respectively. The abscissae show the time since the start of the observation, in seconds. The ordinates show the count rate, in counts s^{-1}. The three solid lines in each graph on the left-hand panels indicate the mean and (mean $\pm$ 20 per cent) high-energy count rates. The long-dashed lines show the same quantities with the median. The two short-dashed lines delimit the 'normal' range of count rates reported by Nevalainen et al. (2005), which is exceeded during most of this observation. On the right-hand panels, the solid (long-dashed) lines delimit the acceptable range of count rates computed with the mean (median), according to Nevalainen et al. (2005). The short-dashed lines delimit the 'normal' range observed by Nevalainen et al. (2005); only the top line is seen in the top two graphs.

caused by the solar wind, which are normally present below 1.0 keV, are not observable. To assess the amount of thermal emission from the halo in our source region for 1401−33, we made the assumption that the thermal emission is spherically symmetric about the centre of the cluster (i.e. NGC 5419), and chose a local background region equidistant from the centre of the thermal emission as the source region. Our assumption is based on a previous X-ray observation of the cluster with the *ROSAT* PSPC (in which IC/CMB emission from the relic was not detected); fig. 8 in Subrahmanyan et al. (2003) is an X-ray image from the observation, showing rotationally symmetric contours about NGC 5419. The regular symmetric shape of the cluster justifies our choice of the background region. In addition, Subrahmanyan et al. (2003) also revealed that a large portion of the *XMM–Newton* field of view in our observation overlaps with the extent of the radio source at 330 MHz. Thus, we chose a circular region just to the north of the target, instead of the usual annulus surrounding the source region. Fig. 2 shows the resulting background region, with the extent of the 330-MHz emission for reference. To calculate the local background event rate and its variation, we applied the background region to the filtered image and exposure map, and obtained additional background regions, following the same recipe as outlined above for 0917+75.

Because our background region for 1401−33 is not close to the centre of the telescopes' field of view, vignetting is a potential issue. Pradas & Kerp (2005) reported an overcorrection of vignetting towards the rim of each detector by the routine eexpmap that generates exposure maps in SAS versions 5.3.3 and 5.4.1. To avoid overlapping with the extent of the radio emission of 1401−33 at 330 MHz, we have no choice but to place our background region at the periphery of the *XMM–Newton* field of view. Thus, the overcorrection of vignetting affects our analysis, potentially overestimating the count rate in the background region. On the other hand, the particle background that dominates at high energies is not vignetted. To correct for vignetting of the local background properly, we followed a two-step background subtraction method described in appendix A of Arnaud et al. (2002). We calculated event rates in the blank-sky data from Nevalainen et al. (2005) at pixels in the source and background regions and within the optimal energies in this study. We scaled these source- and background-region event rates according to the ratio of hard-band rates in our data and in the blank-sky data. We then subtracted the scaled rates from the event rates in our data to remove the particle background from both the source and background regions. Having eliminated the non-vignetted component, we then scaled the event rate in the background region to the source region according to the ratio of summed exposure in each region, for vignetting correction. Finally, we arrived at the source event rate by subtracting the scaled background-region rate from the source region rate. Table 2 shows the relevant numbers in this analysis.

3.2.3 Flux and field limits

Table 2 summarizes our quantitative results. In this paper, we discuss only results from the MOS detectors, as the MOS and PN results

Table 3. Physical parameters inferred from observations.

Target	0917+75[a]		1401−33[b]		
Measurement	MOS	PN	MOS	PN	
Equipartition: $B_{\rm eq} \mapsto$ flux					
Energy spectral index, α ($S_\nu \propto \nu^{-\alpha}$)	1.0		1.4		
$c_{12}(\alpha)$[c]	9.3×10^7		1.6×10^8		
Radio luminosity, $\log_{10}(L_{\rm r})$[d]	41.4		41.0		erg s^{-1}
Emitting volume, $\log_{10}(V)$[d]	72.4		71.3		cm^3
Magnetic field strength, $B_{\rm eq}$[e]	0.63		1.3		μG
IC/CMB flux (0.3–10 keV)[f]	8.7×10^{-14}		5.5×10^{-13}		erg s^{-1}cm^{-2}
This study: flux $\mapsto B_{\rm measured}$					
Energy spectral index, α ($S_\nu \propto \nu^{-\alpha}$)	1.0		1.4		
$C(\alpha) = \sqrt{c_1}/[4\pi 2^\alpha c_5(2\alpha+1)]$[c]	1.32×10^{31}		1.30×10^{31}		
$G(\alpha)$[f]	0.500		0.653		
Redshift, z	0.125		0.0136		
Synchrotron flux density, $S_{\rm r}(\nu_{\rm r})$	1.2		0.5		Jy
Frequency of radio measurement $\nu_{\rm r}$	0.151		1.49		GHz
3σ IC/CMB flux (0.3–10 keV)	$\leqslant 5.22 \times 10^{-14}$	$\leqslant 1.91 \times 10^{-13}$	$\leqslant 1.47 \times 10^{-13}$	$\leqslant 1.49 \times 10^{-13}$	erg s^{-1}cm^{-2}
$S_{\rm x}\nu_{\rm x}^\alpha = {\rm flux}/\int \nu^{-\alpha}\,{\rm d}\nu$	1.5×10^{-14}	5.4×10^{-14}	4.3×10^{-7}	4.4×10^{-7}	
3σ magnetic field strength, $B_{\rm measured}$[f]	$\geqslant$0.81	$\geqslant$0.42	$\geqslant$2.2	$\geqslant$2.2	μG

[a]Harris et al. (1993). [b]Goss et al. (1987). [c] c_1, $c_5(2\alpha+1)$ and $c_{12}(\alpha)$ are defined by Pacholczyk (1970, appendix 2, p. 231).
[d]Values were from table 4 of Harris et al. (1993), scaled to the currently accepted cosmology. They assumed $H_0 = 50$ km s^{-1} Mpc^{-1}, $q_0 = +0.5$, $\Omega_\Lambda = 0$, a lower cut-off frequency of 10 MHz, and simple spherical and cylindrical geometries for the volumes of emission. The original values were $\log_{10}(L_{\rm r}) = 41.6$, $\log_{10}(V) = 72.8$ and $B_{\rm eq} = 0.5$ μG for 0917+75, and $\log_{10}(L_{\rm r}) = 41.3$, $\log_{10}(V) = 71.7$ and $B_{\rm eq} = 0.8$ μG for 1401−33, although a recalculation gave $B_{\rm eq} = 1.1$ μG for 1401−33 instead.[e]Values were calculated using the classical equipartition formula: $B_{\rm eq} = [\frac{8\pi(1+K)c_{12}L_{\rm r}}{\phi V}]^{2/7}$. [f]Values were calculated using equation (11) in Harris & Grindlay (1979): $B^{\alpha+1} = \frac{(5.05\times10^4)^\alpha C(\alpha)G(\alpha)(1+z)^{\alpha+3}S_{\rm r}\nu_{\rm r}^\alpha}{10^{47}S_{\rm x}\nu_{\rm x}^\alpha}$, with $G(\alpha)$ from table 1 therein.

yield the same conclusions, and the MOS results provide more stringent limits. For 0917+75, the event rates within the source region in the optimal band of 0.2–3.7 keV are 0.0186 and 0.0176 counts s^{-1} for MOS1 and MOS2, respectively, while the corresponding area-scaled event rates in the background regions are (0.0180 ± 0.0016) and (0.0194 ± 0.0015) counts s^{-1}, respectively. For 1401−33, the blank-sky subtracted event rates in the on-axis source region (0.0142 and 0.0168 counts s^{-1}, respectively) are only a fraction of the blank-sky subtracted and area-scaled rates in the off-axis background region [(0.0310 ± 0.0043) and (0.0319 ± 0.0035) counts s^{-1}, respectively]. These numbers, together with the appearance of the X-ray images in Figs 1 and 2, indicate that there is not a detection of the IC/CMB emission from either source.

We converted the measured event rate to the unabsorbed energy flux with PIMMS (Mukai 1993), assuming a power-law spectrum and accounting for redshift and galactic absorption. We set the X-ray spectral index to be the same as the radio spectral index (Harris & Grindlay 1979), assuming any X-ray emission to be IC/CMB in origin. We took the spectral indices ($\alpha = 1.0$ for 0917+75 and 1.4 for 1401−33) and redshifts ($z = 0.125$ and 0.0136, respectively) from previous radio measurements, and the galactic H I column densities (2.09×10^{20} and 5.44×10^{20} cm^{-2}) from the FTOOLS program nH.

To assess the maximum source flux, we adopted three times the rms variation in the local background as an upper limit. When converted to energy flux at 0.3–10.0 keV, the +3σ upper limits are 5.22×10^{-14} erg s^{-1} cm^{-2} for 0917+75 and 1.47×10^{-13} erg s^{-1} cm^{-2} for 1401−33. The measured flux in the source region of 0917+75 is consistent with this 3σ limit, while the source flux for 1401−33 is about 4σ below the measured mean background. Using equation (11) in Harris & Grindlay (1979), and radio measurements reported in Harris et al. (1993) and Goss et al. (1987), we obtained 3σ lower limits on the magnetic field strength at each source; they are 0.81 μG for 0917+75 and 2.2 μG for 1401−33. For comparison, the field strength obtained with the 'classical' equipartition formula (with a low-frequency cut-off of the synchrotron emission at $\nu = 10$ MHz) are 0.63 and 1.3 μG for 0917+75 and 1401−33, respectively. Table 3 provides further details on these calculations. Alternatively, using a revised equipartition formula from Brunetti, Setti & Comastri (1997, equation A4), with the low-energy electron population cut-off at $\gamma_{\rm min} = 1069\sqrt{E_{\rm x,min}/{\rm keV}} = 500$ (Harris & Grindlay 1979) to match the energy range of *XMM–Newton*, and with $D(\delta) \sim 1$, the field strengths are 0.79 and 1.6 μG, respectively. We note, however, that these values are very sensitive to the choice of $\gamma_{\rm min}$, whose true value is unknown without better knowledge of the low-energy synchrotron spectrum.

4 DISCUSSION

In this section, we first discuss each target separately, and then comment on the flux and field limits.

4.1 0917+75

Dewdney et al. (1991) originally thought that 0917+75 was the radio halo of an uncatalogued cluster of galaxies, but Harris et al. (1993) recategorized it as a relic radio galaxy on the basis of its high polarization. It is apparently associated with two galaxies of redshift $z = 0.125$ within the Rood 27 supercluster, whose members include the Abell clusters A762, A786 and A787. Harris et al. (1993) reported a spectral flux density of $S_{\rm r}(\nu_{\rm r}) = (1.2 \pm 0.2)$ Jy at $\nu_{\rm r} = 151$ MHz, and an energy spectral index of $\alpha = 1.0$ at low frequencies, with a spectral break close to 150 MHz. The spectrum flattens to $\alpha = 0.6$ between 325 and 1500 MHz, and steepens again above that. This complex spectral shape could be the superposition of synchrotron

emission from two populations of relativistic electrons; it would be the lower energy population ($478 < \gamma < 3380$, $1 < \nu_r < 48$ MHz) that is responsible for IC/CMB emission in the energy range of *XMM–Newton* (0.2–10.0 keV). Unfortunately, the spatial distribution of the lower energy population is as yet undetermined (below 300 MHz), due to limited angular resolution in low-frequency measurements in the past. In this study, we have made the assumption that the IC/CMB emitting electrons have the same spatial extent as those in the higher energy population, which was given by the NVSS radio maps at 1.4 GHz.

Harris et al. (1995) observed 0917+75 in a 15.8-ks *ROSAT* PSPC observation (with the same assumption on the spatial extent of the IC/CMB electrons). They found the source isolated in X-ray, and not contaminated by thermal emission. They placed a 2σ upper limit of 2.3×10^{-14} erg s^{-1}cm^{-2} (27 counts/15 827 s) on the 0.5–2.0 keV emission from the region. With the better sensitivity of *XMM–Newton*, our result improves on this limit: when converted to 0.5–2.0 keV and 2σ, our upper limit becomes 1.38×10^{-14} erg s^{-1}cm^{-2}. The 2σ minimum magnetic field strength also increases from 0.76 to 0.99 μG, as inferred from this and the radio measurements, but the difference is small compared to uncertainties in the equipartition value of 0.63 μG.

4.2 1401−33

1401−33 extends over a 20 arcmin × 9 arcmin region in the poor cluster Abell S753 around NGC 5419. The morphology is strongly suggestive of a relic radio galaxy. However, the parent galaxy has not been identified. Goss et al. (1987) reported a spectral flux density of $S_r(\nu_r) = 0.5$ Jy at $\nu_r = 1.4$ GHz, with a spectral index of $\alpha = 1.4$. Alternatively, Subrahmanyan et al. (2003) reported $\alpha = 1.4$ between 330 MHz and 1.4 GHz, possibly increasing to $\alpha = 1.9$ between 1.4 and 2.4 GHz, but only for the brightest part of the relic (the 'NE rim', which we consider in this study). When a large area of faint emission to the south-west was included, they reported $\alpha = 2.0$ between 330 MHz and 1.4 GHz, and $\alpha = 2.9$ between 1.4 and 2.4 GHz. To reconcile with an 85-MHz measurement of 57 Jy from 1960, they suggested that there is a spectral break between 100 and 300 MHz. Assuming a break at 165 MHz, $\alpha = 0.7$ below the break frequency.

The only *ROSAT* observations of the region around 1401−33 were offset by 45 arcmin and are both less than 5 ks long, placing no interesting limit on the magnetic field strength. In our observation, we found an elevated flux level in the source region when compared to blank-sky data, but no excess when compared to a local background region equidistant from the bright galaxy NGC 5419. Subrahmanyan et al. (2003) attributed this excess flux to thermal emission from a halo centred at NGC 5419. When we inspect our data with XSPEC, we are able to confirm that this excess emission fits much better to a thermal spectrum than to a power-law spectrum, although the statistics are too low to produce a high-quality fit. The result from this study places a 3σ upper limit on any excess X-ray flux specific to 1401−33 at 1.47×10^{-13} erg s^{-1} cm^{-2} within 0.3–10.0 keV, and a minimum magnetic field of 2.2 μG. These are the first limits on IC/CMB emission reported for 1401−33.

4.3 On the flux and field limits

While the number of known relics has grown beyond 30 (see e.g. Giovannini, Tordi & Feretti 1999; Kempner & Sarazin 2001, for representative samples), studies of their IC/CMB emission remain scarce, and not a single convincing detection has been made so far. Table 4 lists the relics whose IC/CMB emission has been studied, together with the reported field limits. For consistent comparison, we have scaled the equipartition fields from previous studies to the currently acceptable cosmology, but we make no attempt to correct for differences in other parameters (e.g. the frequency band integrated), as the required information is not always available.

There are three claims of possible detections to date, in the Abell clusters A 85, A 754 and A 2034. Bagchi et al. (1998) detect IC/CMB emission from 0038−096 near Abell 85, using the PSPC on *ROSAT*. However, the statistics are poor, and the observation suffers from thermal contamination. More recently, Durret et al. (2005) determine from a more sensitive observation with *XMM–Newton* that the X-ray and radio emissions do not coincide spatially, and that the X-ray spectrum fits equally well to a thermal model with and without an added power-law component. Fusco-Femiano et al. (2003) find non-thermal emission above 45 keV in the aggregate spectrum of A 754 from the PDS on *BeppoSAX*; they attribute it to the central halo and 'east relic' in the cluster, but do not rule out contamination from the radio galaxy 26W 020 in the PDS field of view. Subsequently, Henriksen et al. (2004) are able to account for this hard X-ray component with a power-law model of 26W 020. Finally, Kempner et al. (2003) find weak evidence for IC/CMB emission from the relic in A 2034 with *Chandra*, but comment that the errors

Table 4. List of relics with field limits from published IC/CMB measurements.

Relic	Host cluster	Reference[a]	Classical equipartition z	H_0	B_{eq}(μG) in references[b]	B_{eq}(μG) cosmology updated	$B_{measured}$ (μG)	IC/CMB Instrument	Reference[a]
0038−096	A 85	1	0.0555	100	1.3	1.1(6)	0.95[c]	*ROSAT*	2
'East relic'	A 754	3	0.0542	50	0.3	0.3(3)	0.1[c]	*BeppoSAX*	4
1140+203	A 1367	5	0.022	100	2	1.(8)	>0.84	*RXTE*	6
'A 2034'	A 2034	–	0.113	–	–	–	0.3–0.9[d]	*Chandra*	7
'A 133_7a'	A 133	8	0.0562	75	14.4[e]	14.0	>1.5	*XMM–Newton*	9
1253+275	Coma	10	0.023	50	0.6	0.6(6)	>1.05	*XMM–Newton*	11
0917+75	Rood 27	10	0.125	50	0.5	0.63	>0.81	*XMM–Newton*	12
1401−33	A S753	10	0.0136	50	1.1[f]	1.2(5)	>2.2	*XMM–Newton*	12

[a]References: (1) Feretti & Giovannini 1996; (2) Bagchi et al. 1998; (3) Bacchi et al. 2003; (4) Fusco-Femiano et al. 2003; (5) Gavazzi & Trinchieri 1983; (6) Henriksen & Mushotzky 2001; (7) Kempner et al. 2003; (8) Slee et al. 2001; (9) Fujita et al. 2004; (10) Harris et al. 1993; (11) Feretti & Neumann 2006; (12) this paper. [b]All cited B_{eq} values assume $q_0 = +0.5$, $\Omega_\Lambda = 0$ and H_0 as shown above.
[c]IC/CMB detection has since been refuted by later studies. [d]The authors commented that the errors are 'admittedly quite large.' [e]Minimum energy instead of equipartition is assumed. [f]Recalculation of B_{eq} using luminosity and volume from Ref. (12) gives this value instead 0.8 μG from Ref. (12).

on the measurement are quite large. With the uncertainties in these studies, the nature of IC/CMB emission from relics remains elusive.

While none of the IC/CMB field strengths and upper limits in Table 4 is more than a factor of a few from the values derived from the 'classical' equipartition formula, it is interesting, nevertheless, to note that the three most recent measurements – on 0917+75, 1253+275 and 1401−33 – all give lower limits for the field strength which are slightly larger than the equipartition values. It is as yet unclear whether these deviations are significant, as is evident in the comparison of our field limits with the equipartition values obtained from the revised formula of Brunetti et al. (1997). Both methods of determining the field strength involve parameters with large uncertainties, as we explain below.

The equipartition magnetic field, $B_{\rm eq}$, is given by numerous authors in the past, for instance, as in Harris et al. (1995)

$$B_{\rm eq} = \left[\frac{8\pi(1+K)c_{12}L_{\rm r}}{\phi V}\right]^{2/7},$$

where $L_{\rm r}$ is the radio luminosity, V the emitting volume, K the ratio of proton energy to electron energy, ϕ the filling factor for the emitting plasma and c_{12} a weak function of the spectral index and frequency band. We note that uncertainty in the cosmological distance scale contributes to uncertainty in L/V. In addition, we have assumed the most conservative values for K (=0) and ϕ (=1), which results in high X-ray flux and low B estimates at equipartition. In order to reconcile with the limits imposed by our results, $(1+K)/\phi$ has to be 2.4 times larger for 0917+75 and 6.8 times larger for 1401−33.

In calculating the IC/CMB flux, we have assumed that we can infer the nature of the IC/CMB emitting electrons from past radio observations, while this may not indeed be the case. For instance, although the spectral indices for IC/CMB and synchrotron emissions should be the same, electrons responsible for IC/CMB emission in the energy range of *XMM–Newton* (0.3–10.0 keV) have $586 < \gamma < 3381$, and in a 1-μG magnetic field, they emit synchrotron radiation at frequencies between 1 and 50 MHz, where radio observations are either poor in spatial resolution, or entirely unavailable from Earth, due to reflection off the ionosphere. Thus, we can only rely on extrapolations of the spectral indices at higher frequencies to infer the IC/CMB index. Yet, as is evident from the discussion above, radio spectra of relic galaxies often exhibit complex shapes with multiple breaks. For both 0917+75 and 1401−33, there are indications that a break may exist in their radio spectra between 100 and 300 MHz, and it is not guaranteed that these are the only ones. If the spectrum of a synchrotron source flattens at low frequencies, that would imply lower IC/CMB flux as well, leading to closer agreement of IC/CMB measurements and equipartiton.

Various authors have proposed alternatives to the classical equipartition formula: Brunetti et al. (1997) integrate over a fixed particle energy range instead of a fixed synchrotron frequency range; Beck & Krause (2005) replace the energy density ratio of ions to electrons with their number density ratio, and give estimates of the number density ratio for various types of objects; Pfrommer & Enßlin (2004) consider minimum energy and equipartition criteria in the particular scenario where the synchrotron-emitting electrons are produced in inelastic collisions between cosmic ray protons and ambient thermal gas in the cluster. Yet, uncertainties in the source geometry and electron population can only be resolved with new measurements.

One way to better determine the various uncertain parameters is to make new measurements at as yet unexplored wavelengths. A new generation of low-frequency radio telescope arrays could provide radio measurements of relic galaxies at low frequencies (10–250 MHz) in the future, thus better constraining both the spectral index and spatial extent of IC/CMB emitting particles. Alternatively, a new hard X-ray/soft gamma-ray telescope would enable us to observe the IC/CMB emission by particles whose synchrotron emission is currently observable (particles emitting synchrotron radiation at 330 MHz will emit IC/CMB radiation at 70 keV), thus eliminating the problems of uncertain geometry and an uncertain spectral index. Hard X-ray observations also have the virtue that thermal emission no longer dominates in this energy range, so that sources thermally contaminated in soft X-rays can be observed, substantially increasing the sample size. Better determination of the filling factor ϕ could come from radio measurements of relics with higher angular resolution.

5 SUMMARY

With new X-ray measurements of the two relic sources 0917+75 and 1401−33 using the *XMM–Newton* observatory, we detected no IC/CMB flux from either target. We set the 3σ upper limits on the IC/CMB flux within 0.3–10 keV at 5.22×10^{-14} erg s^{-1} cm^{-2} for 0917+75 and 1.47×10^{-13} erg s^{-1} cm^{-2} for 1401−33. The corresponding 3σ lower limits on their magnetic field strengths are 0.81 and 2.2 μG, respectively, both slightly larger than the classical estimates of the equipartition field. Our study adds to the small sample of relics with limits on their IC/CMB emission. X-ray studies on more relics are needed for a broader picture of this diverse class of radio sources. Further constraints on the particle density and magnetic field strength can be made by IC/CMB measurements at higher X-ray energies (above 10 keV), and by synchrotron measurements at lower radio frequencies (below 300 MHz).

ACKNOWLEDGMENTS

We acknowledge M. Markevitch for discussion on *XMM–Newton* background, and the anonymous reviewer for many constructive suggestions, including the two-step background subtraction method and better presentation of the images in this paper. CMHC thanks Wayne H. Baumgartner for many discussions and advices on SAS, and Ryan C. Ogliore for help interpreting *ACE* data. We thank the *ACE* SWEPAM instrument team and the *ACE* Science Centre for providing the *ACE* data. This research has made use of SAOIMAGE DS9, developed by the Smithsonian Astrophysical Observatory, and of NASA's Astrophysics Data System.

REFERENCES

Arnaud M. et al., 2002, A&A, 390, 27
Bacchi M., Feretti L., Giovannini G., Govoni F., 2003, A&A, 400, 465
Bagchi J., Pislar V., Lima Neto G. B., 1998, MNRAS, 296, L23
Beck R., Krause M., 2005, Astron. Nachr., 326, 414
Brunetti G., Setti G., Comastri A., 1997, A&A, 325, 898
Carter J. A., Read A. M., 2007, A&A, 464, 1155
Condon J. J., Cotton W. D., Greisen E. W., Yin Q. F., Perley R. A., Taylor G. B., Broderick J. J., 1998, AJ, 115, 1693
Croston J. H., Hardcastle M. J., Harris D. E., Belsole E., Birkinshaw M., Worrall D. M., 2005, ApJ, 626, 733
Dewdney P. E., Costain C. H., McHardy I., Willis A. G., Harris D. E., Stern C. P., 1991, ApJS, 76, 1055
Durret F., Lima Neto G. B., Forman W., 2005, A&A, 432, 809
Feretti L., Giovannini G., 1996, in Ekers R. D., Fanti C., Padrielli L., eds, Proc. IAU Symp. 175, Extragalactic Radio Sources. Kluwer, Dordrecht, p. 333
Feretti L., Neumann D. M., 2006, A&A, 450, L21

Fusco-Femiano R., Orlandini M., De Grandi S., Molendi S., Feretti L., Giovannini G., Bacchi M., Govoni F., 2003, A&A, 398, 441
Fujita Y., Sarazin C. L., Reiprich T. H., Andernach H., Ehle M., Murgia M., Rudnick L., Slee O. B., 2004, ApJ, 616, 157
Gavazzi G., Trinchieri G., 1983, ApJ, 270, 410
Giovannini G., Feretti L., 2004, J. Kor. Astron. Soc., 37, 323
Giovannini G., Tordi M., Feretti L., 1999, New Astron., 4, 141
Goss W. M., McAdam W. B., Wellington K. J., Ekers R. D., 1987, MNRAS, 226, 979
Harris D. E., Grindlay J. E., 1979, MNRAS, 188, 25
Harris D. E., Stern C. P., Willis A. G., Dewdney P. E., 1993, AJ, 105, 769
Harris D. E., Willis A. G., Dewdney P. E., Batty J., 1995, MNRAS, 273, 785
Henriksen M., Mushotzky R., 2001, ApJ, 553, 84
Henriksen M., Hudson D. S., Tittley E., 2004, ApJ, 610, 762
Kempner J. C., Sarazin C. L., 2001, ApJ, 548, 639
Kempner J. C., Sarazin C. L., Markevitch M., 2003, ApJ, 593, 291
Kempner J. C., Blanton E. L., Clarke T. E., Enßlin T. A., Johnston-Hollitt M., Rudnick L., 2004, in Reiprich T. H., Kempner J. C., Soker N., eds, The Riddle of Cooling Flows in Galaxies and Clusters of Galaxies. http://www.astro.virginia.edu/coolflow/proc.php
McGlynn T., Scollick K., White N., 1996, in McLean B. J., Payne H. E., eds, Proc. IAU Symp. 179, New Horizons from Multi-Wavelength Sky Surveys. Kluwer, Boston, p. 465
Mukai K., 1993, Legacy, 3, 21
Nevalainen J., Markevitch M., Lumb D., 2005, ApJ, 629, 172
Pacholczyk A. G., 1970, Radio Astrophysics. Freeman & Co., San Francisco
Pfrommer C., Enßlin T. A., 2004, MNRAS, 352, 76
Pradas J., Kerp J., 2005, A&A, 443, 721
Slee O. B., Roy A. L., Murgia M., Andernach H., Ehle M., 2001, AJ, 122, 1172
Snowden S. L., Collier M. R., Kuntz K. D., 2004, ApJ, 610, 1182
Subrahmanyan R., Beasley A. J., Goss W. M., Golap K., Hunstead R. W., 2003, AJ, 125, 1095

This paper has been typeset from a TEX/LATEX file prepared by the author.